Available online at www.sciencedirect.com
ScienceDirect
International Journal of Heat and Mass Transfer 51 (2008) 4228–4237
International Journal of HEAT and MASS TRANSFER
www.elsevier.com/locate/ijhmt

# Experimental characterization of buoyancy- and surface tension-driven convection during the drying of a polymer solution

Guillaume Toussaint, Hugues Bodiguel, Frédéric Doumenc *, Béatrice Guerrier, Catherine Allain [1]

*UPMC Univ Paris 06, Univ Paris-Sud, CNRS, Lab FAST, Bat 502, Campus Univ, Orsay F-91405, France*

Received 2 August 2007; received in revised form 30 January 2008
Available online 11 April 2008

**Abstract**

Within the framework of convection induced by evaporation, an experimental study of the drying of a polymer solution has been performed. Several visualisations of convective pattern development are presented: top view with a video camera and an IR camera, as well as visualisation in a vertical section. The appearance and origin (buoyancy- and/or surface tension-driven instabilities) of the convective structures are analysed as a function of the initial thickness and viscosity. Different regimes are obtained when comparing the lifetime of the convective patterns to the thermal transient regime induced by evaporation and to the formation of a thin viscous skin at the surface.


*Keywords:* Free convection; Evaporation; Polymer solution; Convective patterns

## 1. Introduction

Numerous studies have been devoted to convective patterns induced by evaporation. For a volatile fluid, unlike in standard natural convection experiments [1–6], the vertical temperature gradient results from the evaporation itself and from the coupling between the free surface and the surroundings. If the temperature decrease is large enough, buoyancy forces and surface tension variations may overcome stabilizing forces, and convection begins. The development and evolution of convective patterns induced by evaporation is a complex problem. Indeed, most often convection appears before the system reaches a steady state: starting from an isothermal fluid, the conductive basic temperature profile is nonlinear and time-dependent. This transient regime that is most often not considered in classical stability analysis is specifically addressed by the experiments presented in this paper. Moreover, the thickness of the fluid continuously decreases. In a solution with a nonvolatile solute and a volatile solvent, evaporation decreases the solvent concentration at the surface, and similar instability mechanisms hold for concentration so that coupled thermal and solutal effects may occur. Given these various characteristics (transient regime, coupling with the surroundings, thermo-solutal convection), various experiments as well as stability analyses and numerical simulations have been developed for different configurations, most often focusing on one of the above characteristics only. Among these works, evaporation of a pure fluid taking into account the coupling between the liquid and the gas layers has been studied theoretically and numerically by Merkt and Bestehorn [7], Colinet and co-authors [8], Ozen and Narayanan [9] and Moussy and co-authors [10]. Experiments have been developed by Berg and co-authors [11], Mancini and Maza [12], Colinet and co-authors [8] and Zhang [13]. Coupled

* Corresponding author. Tel.: +33 (0)1 69 15 37 31; fax: +33 (0)1 69 15 80 60.
*E-mail address:* doumenc@fast.u-psud.fr (F. Doumenc).
[1] Catherine Allain, who deceased on October 4th 2006, was involved in most of the work presented in this paper.

0017-9310/$ - see front matter © 2008 Elsevier Ltd. All rights reserved.
doi:10.1016/j.ijheatmasstransfer.2008.02.006

**Nomenclature**

| | |
|---|---|
| $a$ | activity |
| $Bi$ | Biot number $= l/(k \times R_{sup})$ |
| $c$ | heat capacity |
| $D_m$ | mass diffusion coefficient |
| $D_{th}$ | thermal diffusivity |
| $g$ | gravity |
| $h_m$ | mass transfer coefficient |
| $h_{th}$ | heat transfer coefficient |
| $h_{th}^{inf}$ | heat transfer coefficient between the dish bottom and the environment |
| $h_{th}^{sup}$ | heat transfer coefficient between the solution surface and the environment |
| $h_{th}^{tot}$ | total heat transfer coefficient between the sample and the environment |
| $k$ | thermal conductivity |
| $l$ | solution thickness |
| $L$ | vapourization latent heat |
| $Le$ | Lewis number |
| $Ma$ | Marangoni number |
| $M_S$ | solvent molar mass |
| $Pr$ | Prandtl number |
| $P_{VS0}$ | solvent saturated vapour pressure |
| $P_{VS}$ | solution saturated vapour pressure |
| $R$ | gas constant |
| $Ra$ | Rayleigh number |
| $R_{inf}$ | thermal resistance between the dish bottom and the environment |
| $R_{sol}$ | thermal resistance of the solution |
| $R_{sup}$ | thermal resistance between the solution surface and the environment |
| $T$ | temperature |
| $T_{amb}$ | ambient temperature |
| $T_b$ | dish bottom temperature |
| $T_{st}$ | stationary temperature |

*Greek symbols*

| | |
|---|---|
| $\alpha$ | thermal expansion coefficient |
| $\gamma$ | surface tension |
| $\rho$ | density |
| $\mu$ | dynamic viscosity |
| $\omega$ | mass fraction |
| $\Delta T$ | temperature difference between the top and bottom of the solution |
| $\Phi_{th}$ | thermal flux at the free surface |
| $\Psi_m$ | solvent mass flux during the plateau regime |

*Superscripts/subscripts*

| | |
|---|---|
| 0 | initial condition |
| P | polymer |
| S | solvent |

thermal and solutal convection has been considered by Ha and Lai [14] for the evaporation of a droplet and by Bratsun and De Wit [15] for a system without evaporation but with a chemical reaction; the latter shows some analogies with our experiments, since the system evolves in time and may show a succession of surface tension- and buoyancy-driven effects. Transient regime is also taken into account in the study of Kang and Choi [16] for Marangoni convection, and numerical simulations of coupled gravity- and capillarity-driven thermoconvection are presented by Medale and Cerisier [17], but in a nonvolatile fluid.

Beside the fundamental interest of understanding the dominant phenomena in convection induced by evaporation, we emphasize that evaporation takes place in many coating processes and may influence the final state of the sample. The fluid is a solution or a suspension containing the solvent(s) and the material(s) to be coated. In this paper we consider the drying of a polymer solution in order to characterize convection phenomena taking place at the beginning of the drying. In addition to the phenomena mentioned above, another point specific to polymer solutions affects the development of convection: indeed, the change in solvent concentration due to evaporation induces a large change in the solution properties, and especially in the viscosity, so that the ratio between the driving forces (due to buoyancy or surface tension difference) and the viscous forces continuously changes during the drying. Experiments have been performed on a model system, polyisobutylene/toluene, whose thermophysical properties have been previously characterized as a function of solvent concentration. Density and surface tension variations with both the temperature and the concentration lead to an unstable configuration during evaporation. In such a system the determination of the dominant mechanism(s) contributing to convective pattern formation at different times of the drying is a complex problem, and several visualisations (vertical section view and top view with video or IR camera) have been performed to characterize the appearance and evolution of convective patterns during the drying. Pattern morphology as a function of the initial thickness and the initial concentration (i.e. the initial viscosity) are analysed. The existence diagram is compared to an estimation of Rayleigh and Marangoni numbers, and results on the coupling between drying kinetics and evolution of convective patterns are presented.

## 2. System and thermophysical properties

The polymer/solvent solution used is polyisobutylene/toluene. Polyisobutylene (PIB) was supplied by Sigma–Aldrich, with $Mw = 5 \times 10^2$ kg/mol and polydispersity = 2.5. Toluene was supplied by Prolabo (Chromatographic use, purity 99.9%).

Thermophysical properties of the solvent and solute are given in Table 1.

The saturated vapour pressure of the toluene, $P_{VS0}(T)$, can be expressed from the Antoine equation[19]: $\log(P_{VS0}) = A - B/(T + C)$, with $A = 9.0782$, $B = 1343.9$, $C = -53.77$, with $P_{VS0}$ in Pascal and $T$ in Kelvin. The vapourization latent heat is 396 kJ/kg ($T = 298$ K).

The variations with solvent content of the solvent activity, the solution viscosity and the polymer/solvent mutual diffusion coefficient are characteristic of the behaviour of a polymer solution. The activity $a(\omega_S)$ is given in Fig. 1 for $T = 298$ K, where $\omega_S$ is the solvent mass fraction. Experimental points have been obtained from gravimetry experiments in a well-controlled environment [22], and the theoretical curve corresponds to the Flory–Huggins model usually used in polymer solutions [23]. Let us recall that with the assumption of thermodynamic equilibrium at the vapour/solution interface and the assumption of ideal gas for the solvent vapour, the equality of the solvent chemical potentials leads to $a(\omega_S, T) = P_{VS}(\omega_S, T)/P_{VS0}(T)$, where $P_{VS0}$ and $P_{VS}$ are the saturated vapour pressures of the pure solvent and solution, respectively. As can be seen, the activity is greater than 0.9 as long as the solvent mass fraction is greater than about 0.4. That means that the solvent evaporation flux at the beginning of the drying, where convective cells have been observed, is very close to the one obtained with pure solvent evaporation. The mass diffusion coefficient $D_m$ does not change very much for $\omega_S > 0.3$ and is about $10^{-10}$ m$^2$/s. It then decreases by several orders of magnitude when $\omega_S$ decreases and is about $10^{-13}$ m$^2$/s at the end of the drying [22]. Viscosity measurements were performed with a Low Shear 30 rheometer (coaxial cylinders and imposed deformation) [24]. As is well known in polymer solutions, the viscosity strongly depends on solvent content, due to the different arrangements of polymer chains when the solvent concentration changes [25]. The viscosity, which is $0.55 \times 10^{-3}$ Pa s for pure toluene, is about 40 times greater for a polymer mass fraction $\omega_P = 5\%$ ($\mu = 20.8 \times 10^{-3}$ Pa s) and more than 460 times greater for $\omega_P = 10\%$ ($\mu = 255 \times 10^{-3}$ Pa s): cf. Fig. 2. Let us emphasize that the viscosity is very sensitive to solvent content even at large dilutions, while the activity and mass diffusion coefficient do not change much as long as $\omega_S$ is greater than 0.4. Changing the initial polymer concentration then enables the investigation of a large range of Prandtl numbers at the beginning of the drying: Pr is about 6.6 for pure toluene, 250 for $\omega_P = 5\%$, and 3000 for $\omega_P = 10\%$.

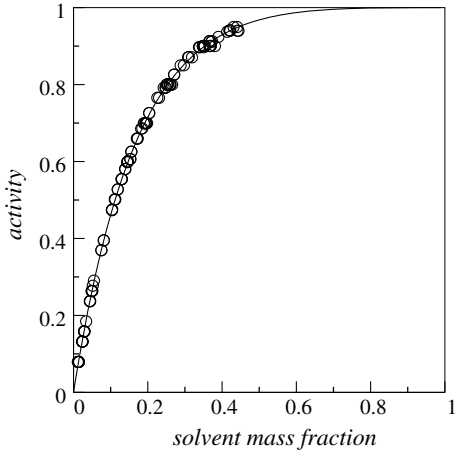


Fig. 1. Activity $a(\omega_S)$ versus solvent mass fraction $\omega_S$ at $T = 298$ K. Open symbols are experimental data [20]. The full line corresponds to the Flory–Huggins fit.

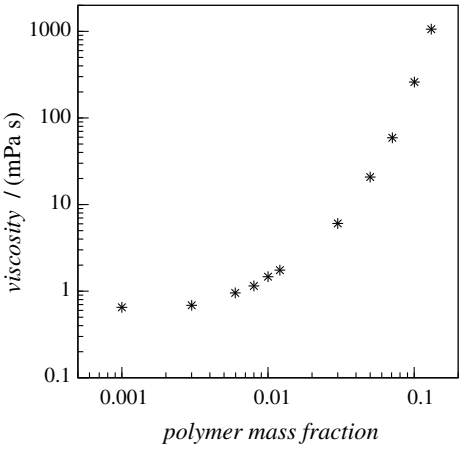


Fig. 2. Viscosity versus polymer mass fraction.

To compare thermal and solutal effects, several points must be taken into account: the maximal temperature variation observed in our experiments is about 5 K, which leads to density and surface tension differences of about 5 kg/m$^3$ and $6 \times 10^{-4}$ N/m, respectively. These values are one order of magnitude smaller than the differences between the density and surface tension of the initial dilute solution and final dry film, so that solutal effects appear more important. On the other hand, the Lewis number that compares the mass to thermal diffusivity is small, $Le \approx 10^{-3}$, so that the behaviours of temperature and concentration fields are very different: the transient thermal

Table 1
Thermophysical properties of toluene and PIB

| | Density $\rho$ (kg/m$^3$) ($T = 293$ K) | $-1/\rho$ (d$\rho$/d$T$)$_P$ Thermal expansion coeff. $\alpha$ (K$^{-1}$) | Surface tension $\gamma$ (N/m) | d$\gamma$/d$T$ (N/(m K)) | Conductivity $k$ (W/(m K)) | Heat capacity $c$ (J/(kg K)) |
|---|---|---|---|---|---|---|
| Tol | 867 [19] | $1.07 \times 10^{-3}$ [19] | $27.92 \times 10^{-3}$ [19] | $-11.9 \times 10^{-5}$ [21] | 0.142 [21] | 1710 [19] |
| PIB | 917 [18] | $5.5 \times 10^{-4}$($T = 300$ K [18]) | $33.6 \times 10^{-3}$ [20] | $-6.4 \times 10^{-5}$ [20] | 0.13 [18] | 1960 [20] |

All the data are given for $T = 298$ K, except where explicitly mentioned.

regime duration is short compared to the time needed to dry the solution, while the concentration gradient evolves during all the drying. This paper deals with the appearance of convective patterns at the very beginning of the drying (quasi-instantaneous or less than 100 s after pouring the solution cf. Section 4.2), so that it mainly concerns the development of thermal instabilities. Experimental results will confirm this assumption.

## 3. Experimental set-up

The solution is poured in a dish and put on a balance (resolution $10^{-7}$ kg) that is located in an extracting hood at room temperature in order to retain organic solvent. Air temperature and solution weight are recorded during the drying process. Evaporation flux used in the following is obtained by derivation of weight measurements. The dish diameter is between $7 \times 10^{-2}$ m and 0.12 m, with most of the experiments being performed in a 0.11 m diameter glass dish. A cylindrical screen is put around the dish in order to limit the perturbation of the air flow on the balance. Preliminary experiments were performed to characterize the boundary conditions. The geometry of the experiment (cylindrical screen) and the air flow produced by the extraction fan induce complex air recirculation above the solution surface. All of the experiments were performed in the same configuration (balance level in the extracting hood, cylindrical screen height) in order to get the same air flow at the solution surface. PIV and anemometry measurements have shown that the air velocity close to the film surface is about 0.1 m/s. The total flow rate in the extracting hood is about 0.05 $m^3$/s, so that solvent concentration can be assumed to be zero far from the solution. Evaporation experiments of pure solvent were performed to estimate global heat and mass transfer coefficients between the sample (solvent + dish) and the environment. The mass transfer coefficient $h_m$ is about $3 \times 10^{-3}$ m/s and the total heat transfer coefficient $h_{th}^{tot}$ is about 30 W/($m^2$ K). A Teflon ring is placed below the dish to isolate it from the balance plate. An estimation of the heat conductance between the dish bottom and the balance gives $h_{th}^{inf} \approx 5$ W/($m^2$ K), so that $h_{th}^{sup} \approx 25$ W/($m^2$ K).

Two parameters have been varied in the experiments: the initial thickness of the solution $l_0(0.3 \times 10^{-3}$–$14.3 \times 10^{-3}$ m) and the initial polymer concentration $\omega_{P0}$(0–15%), which corresponds to an initial viscosity varying from 0.55 to $2100 \times 10^{-3}$ Pa s. Let us emphasize that a very interesting point with such a system is that the investigation of a large domain of Prandtl, Rayleigh and Marangoni numbers is possible.

Several means of observation have been used to characterize the convection patterns as shown in Fig. 3. Top views were performed with a Marlin digital camera, the solution being seeded with iriodin particles [26]. These small flakes are flat and stretched particles (about 10 μm in the largest dimension) and move towards the flow direction. They are bright when the flow is horizontal and dark when the flow is vertical. For a few experiments top views were also performed with an IR camera (CEDIP camera, resolution 20 mK). The two kinds of visualisation are similar with respect to characterization of convective patterns, but the IR camera is more sensitive and gives information on the whole surface temperature field. For a few experiments, observations in a vertical plane were also made using a laser sheet and silvered hollow glass spheres as tracers (diameter 10 μm, supplied by Dantec Dynamics). For practical reasons the digital camera has to be tilted compared to the laser sheet as shown in Fig. 3. Due to the refraction at the interface, images are distorted and a preliminary visualisation with a test grid in toluene was performed to calculate real vertical and horizontal dimensions from distorted images.

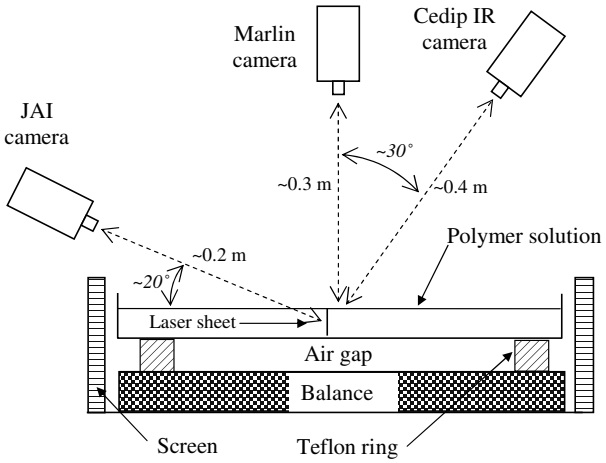


Fig. 3. Visualisation. Top view: Marlin digital camera (640 × 480 pixels, focal length $12 \times 10^{-3}$ m, acquisition rate: 1–4 images/s) and CEDIP IR camera (InSb sensor, thermal resolution 20 mK, 320 × 256 pixels, focal length $27 \times 10^{-3}$ m, acquisition rate: 25 images/s). Vertical section visualisation: JAI digital camera (1600 × 1200 pixels, focal length $60 \times 10^{-3}$ m, acquisition rate: 1–4 images/s). The laser sheet is $2 \times 10^{-3}$ m thick (He–Ne 6 mW laser).

## 4. Results and discussion

### 4.1. Kinetics

Typical kinetics corresponding to the configuration $l_0 = 4 \times 10^{-3}$ m and $\omega_{P0} = 5\%$ are given in Fig. 4. As long as the solvent volume fraction at the surface is greater than 0.4, the evaporation is quite similar to the evaporation of pure solvent (cf. thermophysical properties section): starting from the ambient temperature, the solvent evaporation induces a decrease of the solution temperature, and the kinetics first show a decreasing flux over about 1000 s, corresponding to the time needed by the surface to reach its steady temperature $T_{st}$. Subsequently, the evaporation flux is nearly constant. Let us recall that in the experimental set-up the temperature at the bottom of the dish is not externally controlled but results from the exchange with the surroundings, with $h_{th}^{inf} \approx 5$ W/($m^2$ K). The temperature

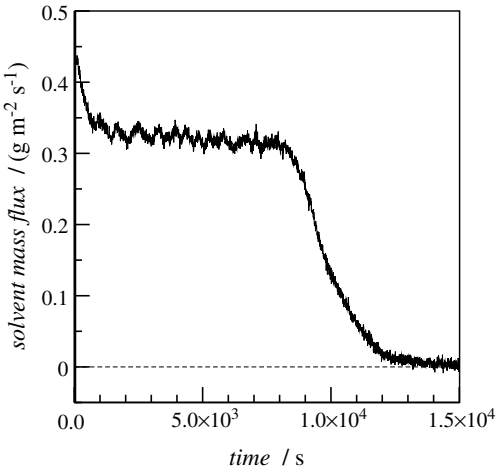


Fig. 4. Solvent evaporation flux for the configuration $l_0 = 4 \times 10^{-3}$ m and $\omega_{P0} = 5\%$.

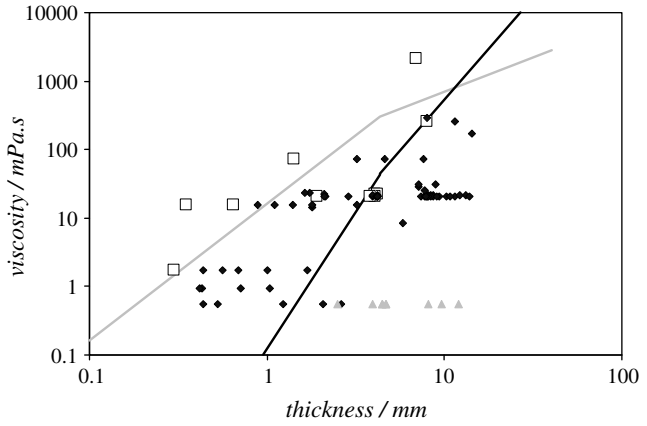


Fig. 5. Existence diagram of convective patterns. Open squares = no convection; black diamonds = cells or rolls; grey triangles = turbulent convection. Marangoni threshold $Ma = 100$: grey line; Rayleigh threshold $Ra = 1000$: black line.

difference between the surface ($T_{st}$) and the bottom ($T_b$) at the end of the thermal transient regime is then given by $(T_{st} - T_b) = (T_b - T_{amb}) \times (l \times h_{th}^{inf})/k$, where $T_{amb}$ is the ambient temperature in the extracting hood and $l$ the solution thickness.

When the solvent concentration becomes small across the whole thickness, the evaporation flux strongly decreases ($t > 8000$ s in Fig. 4) and the end of the drying is very slow, due to the small value of the mass diffusion coefficient at low solvent concentration. The viscosity is then too large for convection to be active and the transfer is only diffusive. Let us note that for some configurations, wrinkles form on the film [24,27]. They appear during the drop in the evaporation flux, well after the end of convection. They will not be considered in this paper, which concerns convection phenomena observed at the beginning of the drying.

### 4.2. Existence diagram and time of appearance

An overview of the existence diagram is given in Fig. 5 for the various initial thicknesses and viscosities tested. Independently of the lifetimes of convective patterns that are analysed in the next section, this diagram shows which configurations are unstable, i.e. which thickness and viscosity lead to a temperature gradient large enough for capillary and/or buoyancy forces to overcome viscous forces during some period of the drying. The grey triangles (pure toluene and large thicknesses) correspond to turbulent convection (the observed structures move very fast), the black diamonds to convective patterns, and the open squares to experiments where no convection was observed. Convective patterns, when observed, always appear at the very beginning of the drying: they are quasi-instantaneous for the smallest viscosities and appear at times up to 100 s for the largest ones. The thickness and mean viscosity variations between the beginning of the drying and the beginning of convection are then very small (typically $10^{-5}$ m for the thickness and 1% for the viscosity), so that the initial values $l_0$ and $\mu_0$ can be used to estimate stability thresholds for the onset of convection.

### 4.3. Thresholds estimation

As previously stated, given the small value of the Lewis number and the time at which convective patterns appear, the development of thermal instabilities are more likely than solutal instabilities to explain the observed phenomena at the beginning of the drying. This assumption will be discussed later. A complete stability analysis would be complex due to the inherent transient character of the problem. In this paper, mainly dedicated to experimental results, we limit ourselves to the estimation of the order of magnitude of thermal Rayleigh and Marangoni numbers with

$$Ra = (\alpha \Delta T \rho g l^3)/(\mu D_{th}), \quad Ma = [(d\gamma/dT)\Delta T l]/(\mu D_{th}).$$

The following approximations have been used: the thickness used in the estimation of $Ra$ and $Ma$ is the entire thickness of the solution, since convection cells have been observed over the whole height (large $Pr$ number). Convection occurs at the beginning of the drying so that the solvent content is large, and we have used for $\alpha$, $d\gamma/dT$ and $D_{th}$ the values of toluene (cf. Table 1), and for $l$ and $\mu$ the initial values, $l_0$ and $\mu_0$. The approximation of the temperature difference $\Delta T$ between the top and bottom of the solution is deduced from a purely diffusive model (i.e. before the convection starts).

Starting from the initial temperature (i.e. the ambient air temperature), solvent evaporation decreases the surface temperature down to a stationary value $T_{st}$, which is constant during the "plateau" regime of the drying kinetics (cf. the kinetics section). This temperature can be easily deduced from the energetic balance. The following notations are used: $R_{sup}$ is the thermal resistance between the film surface and the ambient air (dominated by convection in the hood air, $R_{sup} = 1/h_{th}^{sup}$), $R_{sol}$ is the thermal resistance

of the solution ($R_{sol} = l/k$), and $R_{inf}$ is the thermal resistance between the bottom of the solution and the balance ($R_{inf} = 1/h_{th}^{inf}$, neglecting the 2 mm glass dish thermal resistance). Because $R_{sup}$ is much smaller than ($R_{sol} + R_{inf}$), the heat flux needed to evaporate the solvent in the steady state is mainly due to the exchange of the surface with the ambient air: $T_{amb} - T_{st} \approx R_{sup} \times L \times \Psi_m$, where $\Psi_m$ is the solvent mass flux during the plateau regime: $\Psi_m = (h_m \times P_{VS0}(T_{st}) \times M_S)/(R \times T_{st})$, where $M_S$ is the solvent molar mass and $R$ the gas constant. Given the solvent mass flux obtained in the experiments, $T_{amb} - T_{st}$ is about 5 °C.

During the transient thermal regime two cases must be considered, depending on the ratio between $\tau_1$, the time needed by the thermal perturbation to reach the bottom of the dish, and $\tau_2$, the characteristic time needed by the surface to reach $T_{st}$. $\tau_1$ is the characteristic time of diffusion in the solution, $\tau_1 = l^2/D_{th}$. $\tau_2$ may be deduced from a model of semi-infinite medium: $\tau_2 = (k \times \rho \times c)/(h_{th}^{sup})^2$. The ratio $\tau_1/\tau_2$ is then equal to $Bi^2$, with $Bi = l/(k \times R_{sup})$.

For a large Biot number, $\tau_1/\tau_2 = Bi^2 \gg 1$, the surface is close to the stationary temperature $T_{st}$, while the bottom of the dish is still at the initial temperature. In that case, the estimation of $Ra$ and $Ma$ is made using $\Delta T = T_{amb} - T_{st}$.

For a small Biot number, the thermal perturbation reaches the bottom of the dish before the surface temperature attains $T_{st}$. $\Delta T$ is then smaller than in the previous case. Assuming that at the beginning of the transient regime the surface temperature is close to the ambient temperature, the heat flux needed to evaporate the solvent is mainly due to diffusion in the solution and $\Delta T$ is approximated by: $\Delta T = \Psi_m \times L \times (k/l) = (T_{amb} - T_{st}) \times Bi$. In the case of small Biot number, $Ra$ is proportional to $l^4$ and $Ma$ to $l^2$, while in the case of large Biot number the dependence is in $l^3$ and $l$ for $Ra$ and $Ma$, respectively. The transition between the two regimes is obtained for $Bi = 1$, that is $l \sim 5 \times 10^{-3}$ m.

Let us note that given the range of thicknesses and viscosities used in the experiments, several orders of magnitude of $Ra$ and $Ma$ numbers are explored, from about 10 to $10^6$. Instability thresholds are drawn in Fig. 5, using the following values: for Rayleigh–Bénard instabilities, the onset threshold does not depend much on the boundary conditions, and the order of magnitude of the critical $Ra$ number is 1000 in classical configurations [28]. In the case of Bénard–Marangoni instabilities, convection is induced by heterogeneities of surface tension (due to heterogeneities of surface temperature) and then the critical $Ma$ number is more sensitive to the Biot number. Moreover, when evaporation occurs, stability analyses show that the threshold also depends on the evaporation flux (cf. [7] for more details). The thermal flux at the surface is expressed as

$$\Phi_{th} = h_{th}^{sup}(T - T_{amb}) + L\Psi_m(T) \approx [h_{th}^{sup} + L(\partial\Psi_m/\partial T)](T - T_{amb}) + L\Psi_m(T_{amb}),$$

where $L$ is the latent heat and $T$ the surface temperature. The effective Biot number is then given by

$Bi^{evap} = [h_{th}^{sup} + L(\partial\Psi_m/\partial T)] \times l/k$ [7].

In our case the heat transfer coefficient $h_{th}^{sup}$ is large compared to $L(\partial\Psi_m/\partial T)$ (forced convection in the extracting hood) and $Bi^{evap}$ is about $180 \times l$, with $l$ (m) the solution thickness. Then the effective Biot number is of the order of unity (or smaller), which corresponds to a critical Marangoni number of about 100. The straight lines in Fig. 5 correspond to the two onsets, $Ra = 1000$ (black line) and $Ma = 100$ (grey line). They are noted RB (Rayleigh–Bénard) and BM (Bénard–Marangoni) thresholds in the following. The experimental results are consistent with the onset values and no convective patterns are observed below the thresholds. On the right hand side of the BM threshold, there are a few configurations for which no patterns are observed; these configurations are discussed later. As a first conclusion, the estimation of $Ra$ and $Ma$ numbers and the use of usual thresholds appear to be in good agreement with observed instabilities. Morphology and evolution of convective patterns are discussed in more detail in the next section.

### 4.4. Time behaviour and pattern morphology

Concerning the lifetime and extinction of convective patterns, several points must be taken into account. First, the temperature gradient evolves during the transient thermal regime. Then, due to solvent evaporation, the thickness decreases and the mean solution viscosity increases. Given the values of the solvent evaporation flux, the rate of the thickness decrease is small (about $3 \times 10^{-7}$ m/s), as are the corresponding rates of change in the mean polymer mass fraction and in the mean viscosity. In addition to stopping convection when the core of the solution becomes too viscous, we point out another effect of the large sensitivity of viscosity to solvent content (cf. Fig. 2). Indeed, the solvent evaporation at the film surface may lead to the formation of a strong concentration gradient close to the interface and the subsequent formation of a thin surface viscous skin, while the viscosity of the bulk is still close to the initial viscosity (cf. experimental visualisation in the following). This surface phenomenon strongly affects the Bénard–Marangoni instability but only weakly the Rayleigh–Bénard one.

Given these points, two domains appear in the "thickness–viscosity" plane that correspond to different morphology and time evolution of convective patterns.

For the configurations included between the two thresholds ($Ma > 100$ and $Ra < 1000$, i.e. experiments between the grey and black lines in Fig. 5), the lifetime of convective patterns is of the same order or smaller than the transient thermal regime. Fig. 6 gives an illustration of this behaviour. The two curves correspond to the temperatures of the centre and the boundary of a convective cell (camera IR top view). The temperature difference between the two points appears at about 35 s, the cell is then active while the mean temperature of the surface decreases (thermal

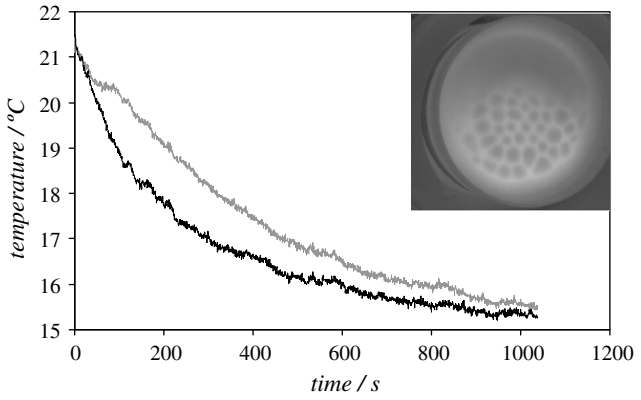


Fig. 6. Camera IR top view at $t = 165$ s ($l_0 = 3.4 \times 10^{-3}$ m, $\omega_{P0} = 7.5\%$) and time evolution of the temperature at the centre (grey line) and boundary (black line) of a convective cell.

transient regime), and convection stops at the end of the transient regime. The hot point is at the centre of the cell, which means that the flow rises from the bottom to the top at the cell centre. This is expected for BM convection, and for RB convection when the viscosity is lower at the bottom [2], which is the case in our problem as the temperature and solvent concentration are smaller at the surface. In this domain the observed patterns are cells (Fig. 7b) whose characteristic lengths may be estimated at the beginning of convection, when they are quite regular and cover the whole dish or a great part of the dish area. Electronic Annex 1 in the online version of this article gives an example of top visualisation performed with the IR camera for the following configuration: $l_0 = 3.4 \times 10^{-3}$ m, $\mu_0 = 15.2 \times 10^{-3}$ Pa s.

The distances recorded in Fig. 8 correspond to the "centre-to-centre" distance of two adjacent cells. In this first domain the wavelength increases with $l_0$ linearly with a slope of about 2.6, close to values observed in classical BM convection [1], and in experiments of pure fluid evaporation [12,13].

As a conclusion, in the first domain corresponding to configurations well below the RB threshold, the thickness

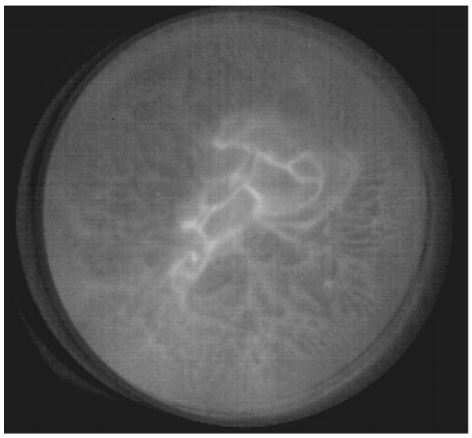

(a) Turbulent structures observed for pure toluene and large thickness:
$l_0$=9.7×10$^{-3}$ m, $\mu_0$=0.55 ×10$^{-3}$ Pa.s.
IR camera, t=103s.

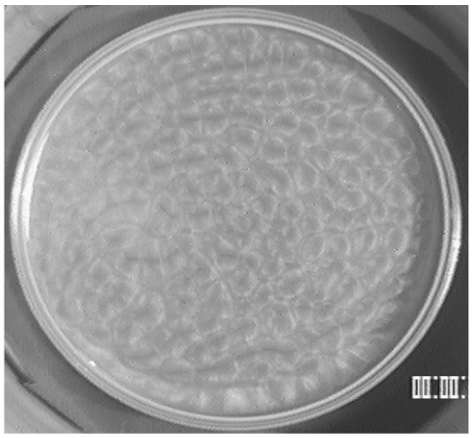

(b) Convective cells
$l_0$=4×10$^{-3}$ m, $\omega_{P0}$=5%, $\mu_0$=20.8 ×10$^{-3}$ Pa.s
Marlin camera, t=37s

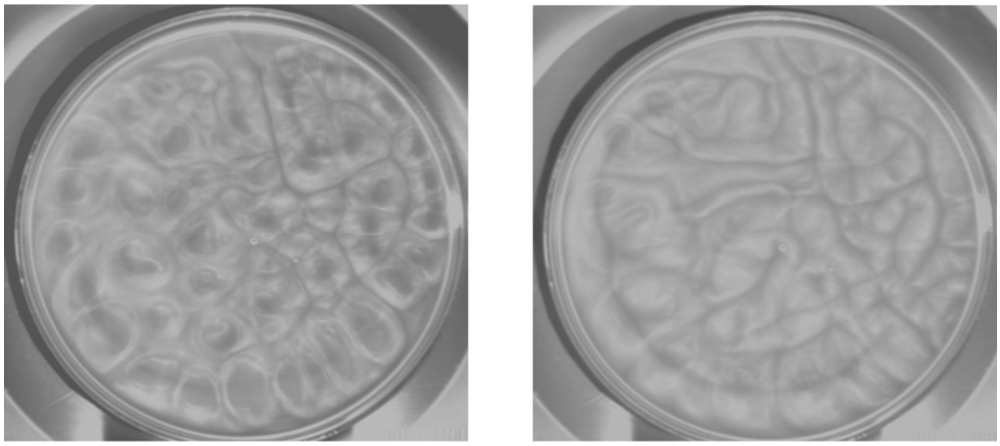

(c) Succession of cells and rolls: $l_0$=8.4×10$^{-3}$ m, $w_{P0}$=5.1%, $\mu_0$=21.5 ×10$^{-3}$ Pa.s
Marlin camera – left: t = 41s; right: t = 109s

Fig. 7. Convective pattern morphology for different thicknesses and viscosities (dish diameter = 0.11 m).

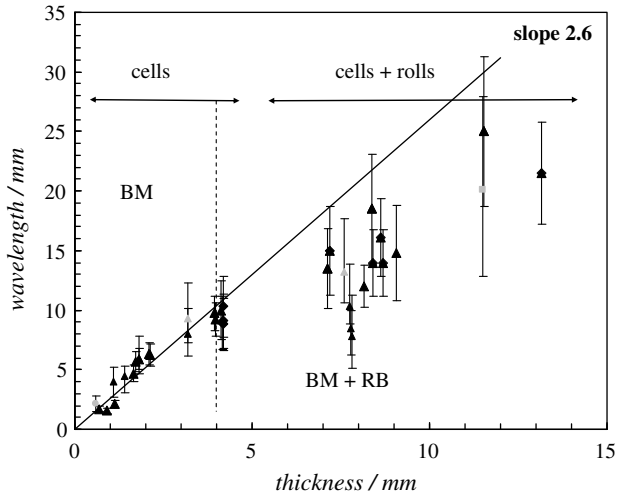


Fig. 8. Characteristic length of convective structures as a function of the initial thickness. Black triangles: $11 < \mu_0 < 35 \times 10^{-3}$ Pa s; grey circle ($l_0 = 0.6 \times 10^{-3}$ m): $\mu_0 = 1.74 \times 10^{-3}$ Pa s; grey triangles ($l_0 = 3.2 \times 10^{-3}$ m and $7.3 \times 10^{-3}$ m): $\mu_0 = 72.6 \times 10^{-3}$ Pa s; grey square ($l_0 = 11.5 \times 10^{-3}$ m): $\mu_0 = 255 \times 10^{-3}$ Pa s. The dashed line indicates boundary of the domains described in Section 4.3.

is not large enough to allow buoyancy-driven convection, and convective cells observed during the transient thermal regime are induced by surface tension. Two mechanisms may be put forward to explain cell extinction: (1) the temperature difference between the surface solution and the bottom of the dish becomes small when the stationary regime is reached, due to the small values of $l$ and $h_{\mathrm{th}}^{\mathrm{inf}}$ (cf. Section 4.1); (2) the instability driven by surface tension may be stopped by the formation of a viscous surface skin.

Let us also note that in this domain, and for similar experiments, convection may not appear or may be sometimes limited to fleeting patterns (cf. superposed open squares and black diamonds in Fig. 5). These experiments are beyond the BM threshold, so that at least surface tension-driven convection should be expected. Here again two arguments may be suggested to explain the lack of reproducibility. First, Marangoni experiments are very sensitive to surface pollution which changes the surface tension and subsequently affects the driving force. Another interpretation could also be that the formation of the viscous skin stops the Marangoni cells. In the opposite way, convection brings dilute solution towards the surface and prevents the skin formation. If none of these two antagonist effects clearly dominates for that range of thicknesses, convection may or may not begin.

Actual experimental results do not provide conclusions regarding the dominant mechanisms responsible for cell extinction and the lack of reproducibility in this first domain. A numerical simulation taking into account both the transient regime and the evolution of solution properties would likely provide further understanding on pattern evolution.

The second domain corresponds to the configurations above the RB threshold: in that case convection is always active after the end of the thermal transient time. In this domain the transient and stationary thermal regimes lead to a temperature gradient large enough to produce convection. Convection stops because of the thickness reduction and because of the viscosity increase, which is due to the decrease in solvent concentration. Morphologies are also different from the previous case: for pure toluene ($\mu_0 = 0.55 \times 10^{-3}$ Pa s) no stable patterns are observed (turbulent regime, Fig. 7a). For larger viscosities, rolls or a succession of cells and rolls are obtained (Fig. 7c). Except for the turbulent structures where no wavelength can be defined (grey triangles in Fig. 5), the characteristic lengths as a function of the initial thickness have been estimated as previously, i.e. at the beginning of convection. They correspond to the "centre-to-centre" distance of two adjacent cells or to the distance between the axes of two co-rotative rolls. As can be seen in Fig. 8, the slope of 2.6 does not apply anymore indicating another regime than the one in the first domain. Skin formation was observed for several experiments using tracers spread on the surface at different times of the drying (see Fig. 9). The skin formation was observed well before the end of convection. For example, in several experiments corresponding to the configuration "$l_0 \sim 8 \times 10^{-3}$ m and $\mu_0 \sim 25 \times 10^{-3}$ Pa s", the skin

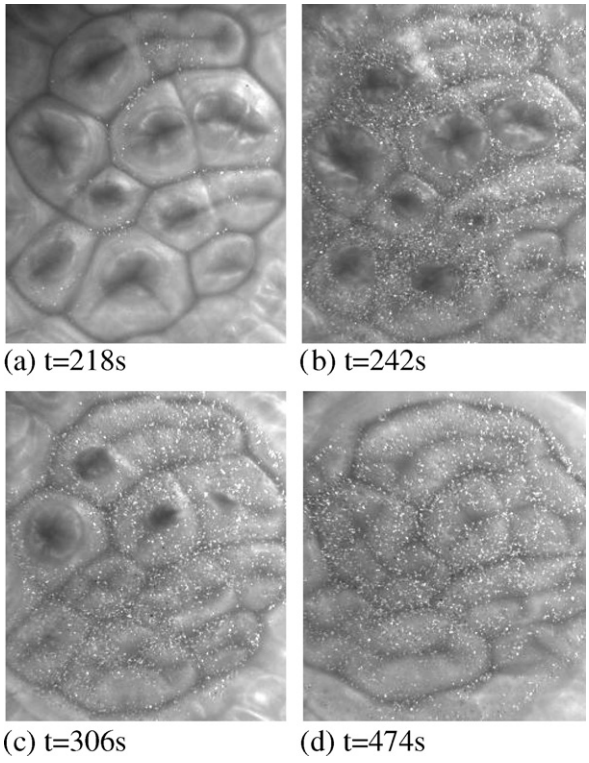


Fig. 9. Skin formation. Zoom on a few cells at four successive times for the configuration: $l_0 = 7.80 \times 10^{-3}$ m, $\mu_0 = 21.0 \times 10^{-3}$ Pa s. The surface is spread with aluminium powder between photos (a) and (b); photo (b): the aluminium powder had converged at the boundary of convective cells where the skin begins to form; photos (c) and (d): the skin overruns the whole surface, while convection is still active under the thin viscous skin. For photo (d), the thickness is $7.55 \times 10^{-3}$ m and the mean viscosity is $22.6 \times 10^{-3}$ Pa s. (a) $t = 218$ s, (b) $t = 242$ s, (c) $t = 306$ s, (d) $t = 474$ s.

appears at about 200 s, while convection ends between $10^3$ and $10^4$ s. Tracer movements on the surface and comparison of surface and internal velocities (obtained from visualisation in a vertical section) show that the motions in the two zones are not correlated, which indicates that the convection observed in the bulk is only induced by buoyancy for times greater than about 200 s.

Given the time scale involved, one may also wonder if the assumption that convection is dominated by thermal rather than solutal effects is still valid. In order to confirm this point, some experiments were performed using deuterated toluene ($C_7D_8$, supplied by Euriso-top) as solvent instead of toluene ($C_7H_8$). Because the density of deuterated toluene is 940 kg/m$^3$, the density difference between PIB and solvent is reversed. Therefore, the evaporation that concentrates the polymer near the surface is no longer an unstable configuration in terms of solutal gravitational instability. Except for the density, the other properties of the solvent are nearly unchanged so that this experiment allows a precise comparison of the two systems. Experimental results show no significant differences when using deuterated toluene: convection patterns observed for the two solvents (toluene and deuterated toluene) are similar, as can be seen in Fig. 10. Moreover, the order of magnitude of the velocity determined from visualisation in a vertical section is the same, so that solutal density difference is clearly not the dominating parameter.

Collecting all these results leads to the following conclusion for the configurations above the RB threshold: for large thicknesses, evaporation induces thermal convection that first appears during the transient thermal regime, due to surface tension and/or density gradients, and then continues during the stationary regime, due to thermal buoyancy forces, below a thin viscous skin that covers the film surface.

## 5. Conclusion

Experiments of polymer solution dryings have been performed for a large domain of initial thicknesses and viscosities. Information from several kinds of visualisations and comparison with Rayleigh and Marangoni thresholds have provided an understanding of the complex behaviour of the observed convection and revealed the dominant mechanisms, due here to thermal density or surface tension gradients. One specific feature of this problem is the transient character of the convection, in the sense that the lifetime of the convective patterns is small compared to the whole drying time. For small thicknesses, cell patterns induced by surface tension disappear before the end of the thermal transient regime. For large thicknesses, convection starts during the transient regime but lasts much longer. In this case, the end of convection is due to the increasing viscosity and decreasing thickness of the solution. In the domain of large thicknesses, a succession of cells and rolls has been most often observed and after a few hundred seconds, only buoyancy-driven convection is active under a thin viscous polymer concentrated skin that has overrun the whole surface. Coupling between the convection and skin formation is a complex problem that would be interesting to study in more detail. Comparison with theoretical stability analysis as well as numerical simulations will yield very interesting information on the relative importance of the parameters. In addition, the possible influence of convection on the final state of the film is another important question, especially for application purposes.

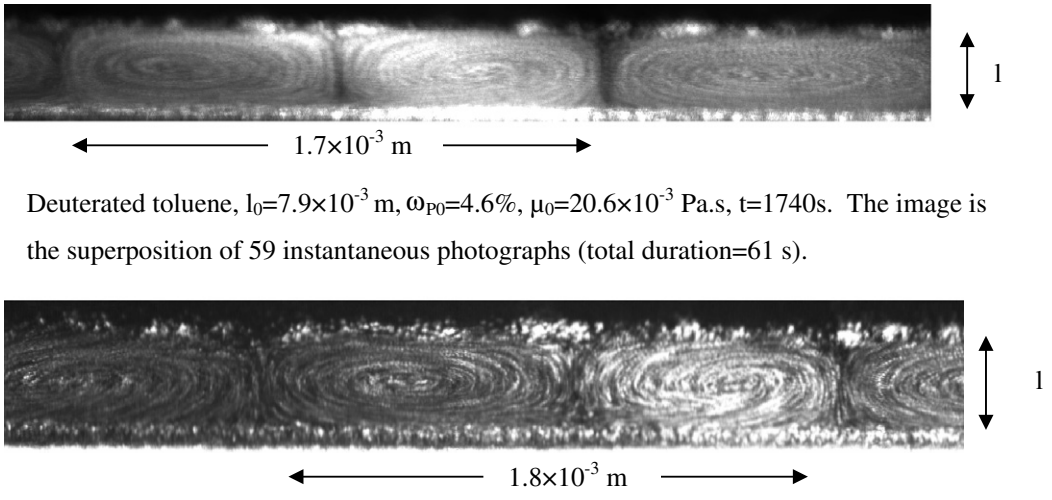


Deuterated toluene, $l_0=7.9\times10^{-3}$ m, $\omega_{P0}=4.6\%$, $\mu_0=20.6\times10^{-3}$ Pa.s, t=1740s. The image is the superposition of 59 instantaneous photographs (total duration=61 s).

Toluene, $l_0=8.0\times10^{-3}$m, $\omega_{P0}=5\%$, $\mu_0=20.9\times10^{-3}$ Pa.s, t=1740s. The image is the superposition of 30 instantaneous photographs (total duration=30 s)

Fig. 10. Comparison of convection patterns for toluene and deuterated toluene. Visualisation in a vertical section (laser sheet, cf. Fig. 3). The maximal horizontal velocity is about $0.25\times10^{-3}$ m/s.

## Acknowledgments

The authors thank M. Rossi from "Institut Jean Le Rond d'Alembert, CNRS-UPMC" for helpful discussions. This work was partly supported by the "Agence Nationale de la Recherche, France" (ANR-05-P-BLAN-0056-01) and by the "Fédération TMC (Ministère de l'Enseignement supérieur et de la Recherche, France)".

## Appendix A. Supplementary data

Supplementary data associated with this article can be found, in the online version, at doi:10.1016/j.ijheatmasstransfer.2008.02.006.

## References

[1] J.R.A. Pearson, On convection cells induced by surface tension, J. Fluid Mech. 4 (1958) 489–500.
[2] F.H. Busse, Non-linear properties of thermal convection, Rep. Prog. Phys. 41 (1978) 1930–1967.
[3] J. Reichenbach, H. Linde, Linear perturbation analysis of surface tension driven convection at a plane interface, J. Colloid Interf. Sci. (1981).
[4] D.A. Goussis, R.E. Kelly, On the thermocapillary instabilities in a liquid layer heated from below, Int. J. Heat Mass Transfer 33 (1990) 2237–2245.
[5] P. Colinet, J.C. Legros, M.G. Velarde, Nonlinear Dynamics of Surface-Tension-Driven Instabilities, Wiley-VCH, 2001.
[6] P. Manneville, Rayleigh–Bénard convection, thirty years of experimental, theoretical, and modelling work, in: I. Mutabazi, E. Guyon, J.E. Wesfreid (Eds.), Dynamics of Spatio-temporal Cellular Structures, Henri Bénard Centenary Review, Springer Tracts in Modern Physics, 2006.
[7] D. Merkt, M. Bestehorn, Bénard–Marangoni convection in a strongly evaporating fluid, Physica D 185 (2003) 196–208.
[8] P. Colinet, L. Joannes, C.S. Iorio, B. Haut, M. Bestehorn, G. Lebon, J.C. Legros, Interfacial turbulence in evaporating liquids: theory and preliminary results of the ITEL-MASER 9 sounding rocket experiment, Adv. Space Res. 32 (2) (2003) 119–127.
[9] O. Ozen, R. Narayanan, The physics of evaporative and convective instabilities in bilayer systems: linear theory, Phys. Fluids 16 (12) (2004) 4644–4652.
[10] C. Moussy, G. Lebon, J. Margerit, Influence of evaporation on Bénard–Marangoni instability in a liquid–gas bilayer with a deformable interface, Eur. Phys. J. B 40 (2004) 327–335.
[11] J.C. Berg, M. Boudart, A. Acrivos, Natural convection in pools of evaporative liquids, J. Fluid Mech. 24 (1966) 721–735.
[12] H. Mancini, D. Maza, Pattern formation without heating in an evaporative convection experiment, Europhys. Lett. 66 (6) (2004) 812–818.
[13] N. Zhang, Surface tension-driven convection flow in evaporating liquid layers, in: Raffaele Savino (Ed.), Surface Tension-driven Flows and Applications, Research Signpost, 2006.
[14] V-M Ha, C-L Lai, Onset of Marangoni instability of a two-component evaporating droplet, Int. J. Heat Mass Transfer 45 (2002) 5143–5158.
[15] D.A. Bratsun, A. De Wit, On Marangoni convective patterns driven by an exothermic chemical reaction in two-layer systems, Phys. Fluids 16 (4) (2004) 1082–1096.
[16] K.H. Kang, C.K. Choi, A theoretical analysis of the onset of surface-tension-driven convection in a horizontal liquid layer cooled suddenly from above, Phys. Fluids 9 (1997) 7–15.
[17] M. Medale, P. Cerisier, Numerical Simulation of Bénard–Marangoni Convection in small aspect ratio containers, Numer. Heat Transfer. A 42 (2002) 55–72.
[18] G.W. Ver Strate, D.J. Lohse, Polymer Data Handbook, Oxford University Press, 1999.
[19] J.A. Riddick, W.B. Bunger, T.K. Sakano, Organic Solvents Physical Properties and Methods of Purification, John Wiley and Sons, 1986.
[20] J. Brandrup, E.H. Immergut, Polymer Handbook, Wiley Intersciences, 1989.
[21] C. Monteil, M. Postel, K2 constantes, Techniques de l'ingénieur, 1955.
[22] F. Doumenc, B. Guerrier, C. Allain, Mutual diffusion coefficient and vapor–liquid equilibrium data for the system PIB/toluene, J. Chem. Eng. Data 50 (3) (2005) 983–988.
[23] P.J. Flory, Principles of Polymer Chemistry, Cornell University Press, Ithaca, NY, 1953.
[24] Y. Gorand, F. Doumenc, B. Guerrier, C. Allain, Instabilités de plissement lors du séchage de films polymères plans, Rhéologie 3 (2003) 22–29.
[25] M. Doi, S.F. Edwards, The Theory of Polymer Dynamics, Oxford University Press, 1992.
[26] F. Doumenc, C. Iorio, G. Toussaint, B. Scheid, B. Guerrier, C. Allain, Caractérisation expérimentale des instabilités induites par évaporation de solvant dans une solution polymère, in: Proceedings of the Ninth Rencontre du Non-Linéaire, Non-Linéaire Publications, Institut Henri Poincaré Paris, 2006, pp.75–80.
[27] F. Doumenc, B. Guerrier, C. Allain, Surface undulations formed during polymer solution drying, in: CD Proceedings of the IUPAC World Polymer Congress, Paris, 2004.
[28] A. Bejan, Convection Heat Transfer, John Wiley & Sons, 2004.